










STATIC ELASTIC PROPERTIES OF ROCKS OBTAINED BY X-RAY MICROTOMOGRAPHY, INVERSE MODELING AND SURROGATE MODEL

Ruan Gomes^{1,3,4} , Sergio Fontoura^{1,2} , Guilherme Righetto¹ , Luiza Fernandes¹ , Rafael Lopez¹ , Rafaella Sampaio¹ , Claudio Lima⁵ , Marcel Naumann⁶ , William Silva⁵ 

¹Group of Technology in Energy and Petroleum – GTEP/PUC-Rio, Rio de Janeiro, Brazil; ²Department of Civil and Environmental Engineering, Pontifical Catholic University of Rio de Janeiro, Rio de Janeiro, Brazil; ³Water Resources Graduate Program, Oregon State University, Corvallis, Oregon, USA (Current affiliation); ⁴Department of Biological & Ecological Engineering, Oregon State University, Corvallis, Oregon, USA (Current affiliation); ⁵Equinor Research and Technology Center Rio, Rio de Janeiro, Brazil; ⁶Equinor ASA, Stavanger, Norway

Correspondence to:

Ruan Gomes at gomesru@oregonstate.edu

How to Cite:

Gomes, R., Fontoura, S., Righetto, G., Fernandes, L., Lopez, R., Sampaio, R., Lima, C., Naumann, M., & Silva, W. (2025). Static Elastic Properties of Rocks Obtained by X-ray Microtomography, Inverse Modeling and Surrogate Model. *InterPore Journal*, 2(4), IPJ011225-5. <https://doi.org/10.69631/v65nzv74>

RECEIVED: 20 Jan. 2025

ACCEPTED: 14 Oct. 2025

PUBLISHED: 1 Dec. 2025

ABSTRACT

Digital rock analysis uses imaging techniques to obtain information concerning the internal structure of the rock. In the context of obtaining mechanical properties from digital images, much attention is given to determining the elastic parameters of rocks based on their mineralogical composition. While many applications for this type of simulation are available in the literature, the quantification of mineral property variations resulting from external influences has largely been overlooked. This work adopts an inverse modeling approach to estimate such elastic property variations in rocks. This methodology requires a predictive tool and an optimization algorithm to iteratively update the model's parameters while reducing the discrepancies between modeled and measured data. In this study, a representative sandstone sample from the Botucatu Formation in Brazil was used to evaluate the methodology. Two case studies were considered: a synthetic example was designed for validation of the methodology while the second case applies real-world laboratory test data to estimate the properties that are most supported by the experimental evidence. A MATLAB code was built to integrate a finite element program and a genetic algorithm in a single framework. Additionally, an artificial neural network was used as a surrogate model to reduce the computational time of the numerical forward run. Overall, the results support the robustness of the approach and present a new alternative to obtain the mechanical properties of rock constituents at the pore scale.

KEYWORDS

Elastic properties, X-ray microtomography, Inverse modeling, Surrogate model, Pore-scale



@2025 The Authors

This is an open access article published by InterPore under the terms of the Creative Commons Attribution-NonCommercial-NoDerivatives 4.0 International License (CC BY-NC-ND 4.0) (<https://creativecommons.org/licenses/by-nc-nd/4.0/>).

1. INTRODUCTION

Digital Rock Analysis (DRA) uses imaging techniques to help understand and simulate relevant physical processes of rocks (38). This methodology allows a detailed and direct view of the rock's internal microstructure across one or multiple spatial scales (typically between nm to mm scales) (45). Due to its capacity to offer novel perspectives and insights into the study of rocks, this field has experienced a significant surge in popularity in recent decades. Digital rock analysis can serve several purposes, such as facilitating the examination of the internal composition of rocks prior to, subsequent to, or during laboratory studies, hence enabling a deeper understanding of the rock's behavior (8, 29, 30). The digital representation of the rock structure serves well to analyze structural patterns within the rock and can be utilized in conjunction with numerical techniques to simulate particular physical phenomena and derive the relevant material properties (13, 19, 27).

This paper deals with the use of DRA to obtain physical properties, a path that has been followed widely in recent years. The literature provides examples of various applications, including single fluid phase flow (19, 33, 45), multi-phase flow (10, 23), heat transport (11, 17), diffusion (17), reactive transport (14, 16), nuclear magnetic resonance (27), and mechanical responses (13). For these specific applications, it is common to use a digital pore-scale model at a representative spatial resolution to simulate the phenomenon of interest. A model can be assumed representative if the pore-space is sufficiently resolved by the imaging technique and thus porosity and permeability values agree with standard laboratory techniques. Amongst these different applications, our work is particularly focused on a deeper understanding of simulating mechanical responses from digital images.

Mechanical simulations using DRA have been available for decades (3). Recent efforts have been dedicated to simulating static (24) and dynamic (12, 52) conditions for different rock types. These studies, along with others, have a shared goal of determining the elastic parameter of rocks (2, 36, 37). The simulations necessitate the inclusion of the linear elastic properties of the mineralogical elements of the rock as inputs, such as Young's modulus and Poisson ratio. Such values are traditionally standardized representing "intact" minerals, whose interaction with the porous domain of the model provides the elastic property of rocks. While new efforts to extend the linear elastic regime by including damage effects (11) are already available in the literature, the quantification of potential variations in these linear elastic properties, caused by external factors (e.g., weathering due to environmental factors), has received little attention. This paper adopts an inverse modeling approach for better understanding the variability of these properties considering a representative digital sandstone sample.

The methodology proposed in this study is evaluated using a Brazilian sandstone sample, a finite element model, and an optimization technique. The main objective is to develop and validate the inversion strategy within the DRA framework. Additionally, our objective is to determine the degree to which the input attributes of the undamaged minerals accurately reflect the characteristics of this particular rock sample, based on our initial assumptions on the parameters. This assumption is validated by the comparison of observed and simulated datasets. Despite its attractiveness, inverse modelling can be computationally demanding, potentially restricting its practical implementation. There are several strategies available to alleviate this limitation and promote the adoption of this approach. The use of

KEY POINTS:

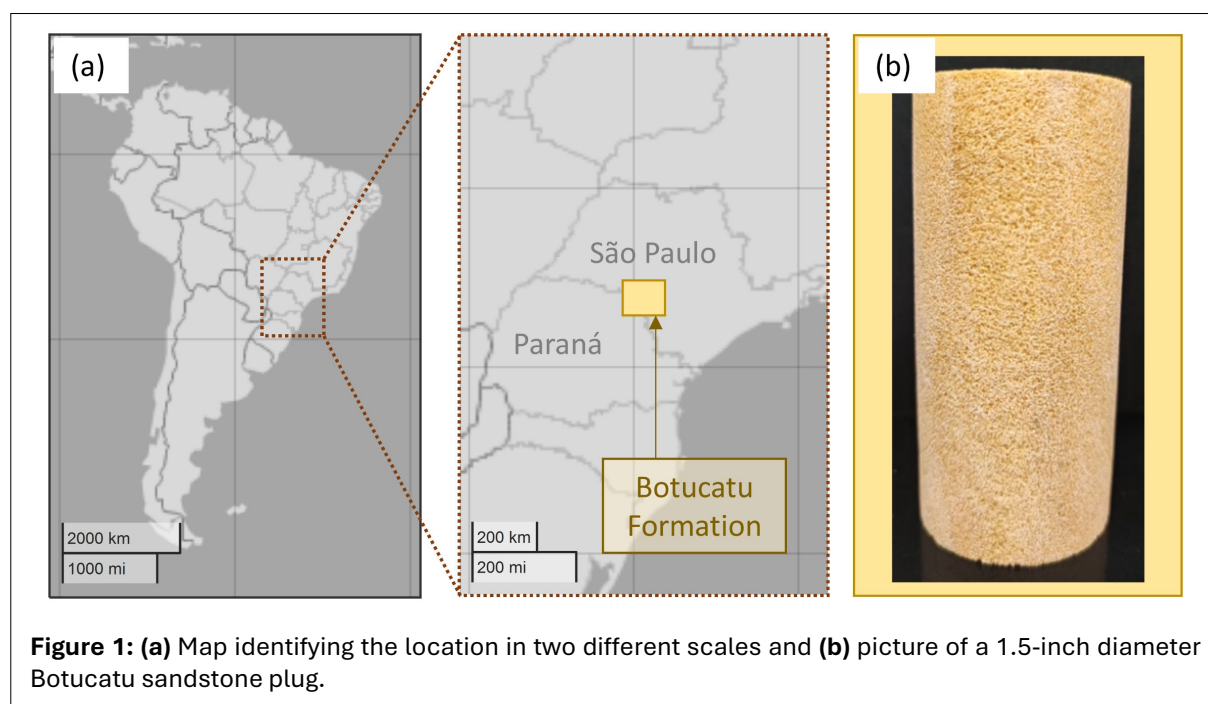
- *Digital Rock Analysis is used to estimate the elastic properties of rocks at the pore scale.*
 - *Unconfined compression test data, x-ray microtomography images, a numerical method, and an optimization algorithm are used to estimate the elastic properties of minerals of a sandstone rock.*
 - *The approach reveals the importance of estimating elastic properties at the pore scale without assuming these represent intact conditions.*
 - *The computational cost of the numerical modeling is improved by including a surrogate model.*
-

surrogate models, also known as emulators, has proven to be advantageous in accomplishing this objective (25).

Machine learning has been frequently used for this purpose due to its ability to learn input-output relationships (4, 18). This paper uses Artificial Neural Networks (ANN) for this task due to their successful application within the context of DRA (50, 51), likewise to its usefulness for predicting responses associated with rock mechanics (34, 42, 53). The proposed methodology thus also evaluates the applicability of ANN as a predictive tool of pore-scale mechanical interactions, in the pursuit of new opportunities for the use of state-of-the-art optimization algorithms and uncertainty quantification.

2. MATERIAL

This work uses a digital pore-scale model of a sandstone sample from the Botucatu formation in Brazil. This rock type is available in the municipality of Ribeirão Claro in the state of Paraná and vicinity regions of the southeast of São Paulo state, as shown in Figure 1a and b. Typically, this rock has porosity values between 20 and 30%, and permeability values ranging between 170 and 2410 mD (7, 32). This rock generally exhibits grains that are rounded in shape, possessing pore diameters that are of a magnitude that can be discerned using X-ray microtomographic methodology. The framework of the Botucatu sandstone primarily consists of quartz (SiO_2) and previous studies (7) have found that the Botucatu sandstone shares similar characteristics with the Berea sandstone, which is widely utilized in the field of DRA modelling (3, 10, 19, 23, 26, 27, 45, 50).

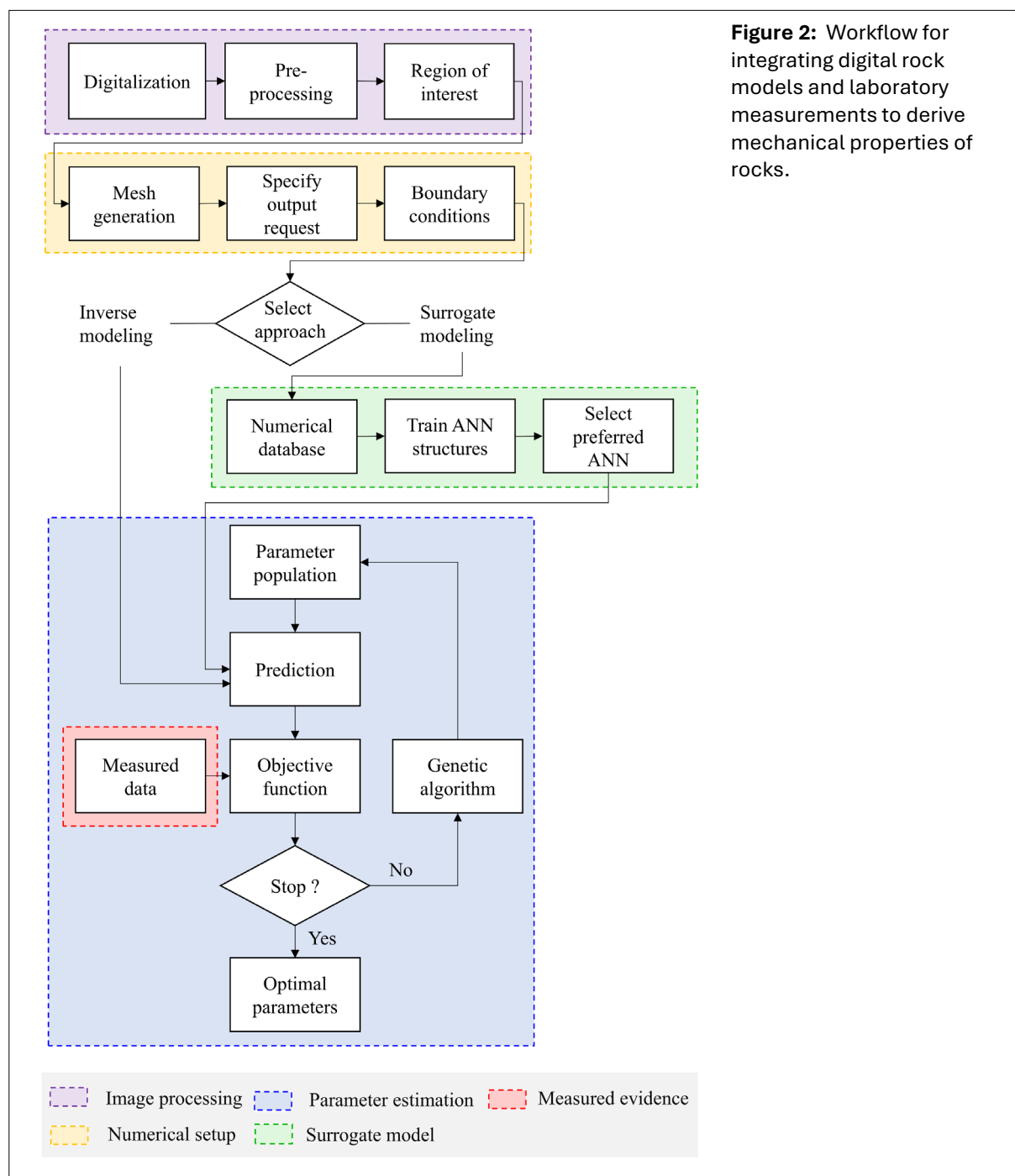


3. METHODOLOGY

This section provides a detailed description of the different building blocks of the proposed methodologies. The various software programs employed in the development of this study are outlined in the respective subsections. It is important to emphasize that the concepts articulated in this protocol possess potential for adaptation to alternative imaging methodologies and software applications. Figure 2 depicts the proposed methodology, and the following subsections provide a detailed description of each component of the workflow.

3.1. Image Processing and Region of Interest

The image processing stage, as indicated in Figure 2 (purple box), comprises three steps: digitalization, pre-processing, and selection of a region of interest.



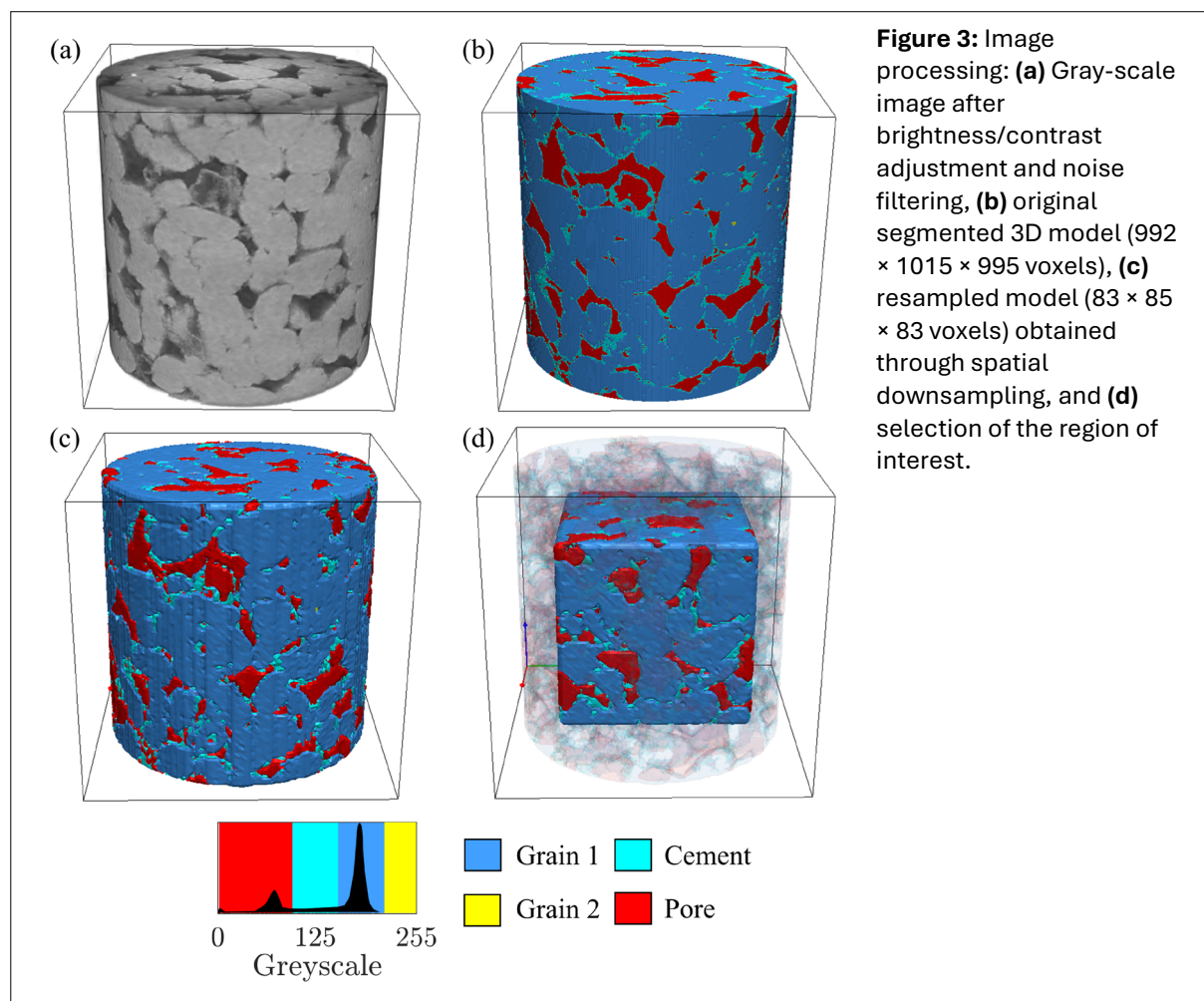
The digitalization step consists of using an imaging technique to scan the rock sample and obtain information on the internal structure in digital format. This work uses X-ray computed microtomography, a technique traditionally used for rock plugs like sandstones and carbonates (9). A high-resolution X-ray microscope^a equipped with an instrument Control System^b was used to digitize the sandstone sample at 1.2 μm resolution, utilizing 100/9 kV/W, 1601 projections, and an exposure time of 6.5 s per projection.

^a ZEISS Xradia 510 Versa: Carl Zeiss X-ray Microscopy, Inc.,
<https://www.zeiss.com/microscopy/en/products/x-ray-microscopy/versaxrm.html>,
https://www.pebrsul.com.br/arquivos/Catalogo_Xradia_510_Versa.pdf

^b Scout-and-Scan™ Instrument Control System (version 14.0):
<https://www.zeiss.com/microscopy/us/l/campaigns/scout-and-scan.html>

The resolution was selected from pore-size distribution data obtained by mercury intrusion porosimetry^c. This data is herein considered instrumental to ensure the selected resolution is sufficient to resolve the pore-space.

The raw images in a grayscale format are subjected to pre-processing: quality enhancement, segmentation, and resampling procedures. A manual brightness and contrast adjustment was performed using a free image processing package^d (15), followed by a Non-local means filter (sigma of 15 and 2 smoothing factors) for denoising. Next, the stacks (2D sections) of images were imported into commercial 3D image-processing software^e (47) to enable proper 3D visualization. Furthermore, a Recursive Gaussian filter (isotropic sigma of 2.3) was used to remove residual noise defects. **Figure 3a** presents the gray-scale 3D model after quality enhancement. Although several segmentation algorithms are available (40), this work employs a manual threshold to distinguish the solid constituents (i.e., minerals) and the pore space, as some minerals in this rock do not exhibit well-defined peaks. **Figure 3b** provides an example of the segmentation process applied to the studied rock, illustrating the four identified phases. The corresponding histogram is shown at the bottom of **Figure 3**. The subsequent step is the resampling procedure. Resampling is used here as a proxy for downsampling and serves as an initial attempt to reduce the computational cost associated with the numerical simulations. The goal



^c Micromeritics AutoPore IV Model 9510, https://micromeritics.com/products/autopore-v/?utm_source=google&utm_medium=cpc&utm_campaign=EN%20-%20Search%20-%20Micromeritics&utm_term=autopore&utm_content=EN%20-%20Product%20-%20AutoPore&gad_source=1&gad_campaignid=22332900911&gclid=Cj0KCQiAoZDJBhCOARIsAERP-F_Cy6woFbjLVAWR9_6N0eWpsvV10C1gTrPkmYmf5EMWqhVW5o1NPckaAou6EALw_wcB

^d Fiji ImageJ: <https://fiji.sc/>

^e Simpleware (version S-2021-06): Synopsys, <https://eval.synopsys.com/Home/Simpleware>

is to achieve a balance between computational cost and the level of detail/information in the model that is deemed important. This step is important as inverse modeling places a heavy demand for computational resources (49). The resampling is conducted in the image processing software using the linear interpolation method. Five downsampling scenarios were considered in this study. The first scenario is referred to as 1X and represents the original model. The remaining scenarios, 2X, 4X, 8X, and 12X, indicate the corresponding downsampling factors. To better illustrate this, consider a 2000^3 voxels image. When downsampling of 2X and 4X is used, the resultant model will have 1000^3 and 500^3 voxels, respectively. **Figure 3b** and **c** illustrate the 3D segmented models before and after downsampling, respectively. Note in **Figure 3** that the details in the downsampled model appear coarser as a result of the interpolation procedure.

The final step of the image processing stage is the selection of a Region of Interest (ROI). In this study, a cubic ROI was used, following a common approach adopted in fluid flow (e.g., 19, 46) and mechanical simulations (e.g., 13, 52). The ROI selection is performed on the 1X model, for which the digital porosity and permeability values agree with laboratory measurements obtained using a gas permeameter^f. In such context, the model is considered a representative elementary volume (5). The same ROI is selected for the downsampling and the rescaling effect in model outputs is tracked in terms of porosity and permeability values. **Figure 3d** illustrates the ROI of the downsampled model.

The entire porous domain and the largest connected network were used to calculate the total and connected porosities, respectively. The connected pore network was used for solving the Stokes equation for flow simulations and the finite element code embedded in the Simpleware FLOW module was used. The voxel finite element (FE)-grid meshing algorithm and solid walls boundary condition were used and the isotropic permeability value was computed. To assess the reliability of the software, we conducted a benchmark study using publicly available rock samples from the Imperial College London database (10). **Figure A1** in the **Supplementary Material** (available online) shows that the adopted software and modeling setup produced permeability estimates in good agreement with well-established approaches, including Lattice Boltzmann (10), pore network modeling (10, 20), and finite difference (19) techniques.

3.2. Numerical Setup

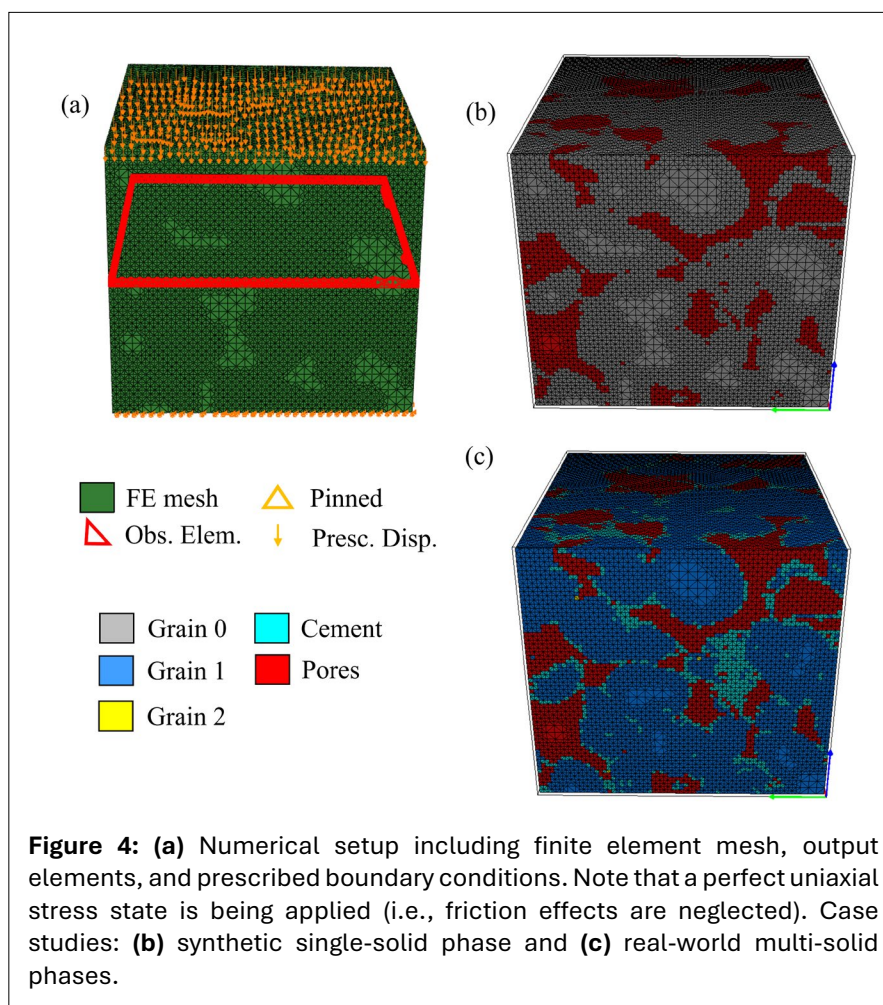
This work adopts the numerical setup corresponding to the unconfined compression test procedure, which is chosen for its ease of implementation in laboratory settings and its potential for accurate numerical replication. Furthermore, it is important to note that while several numerical techniques can be employed, this study specifically utilizes the FE method with the Abaqus (1) software.

Regarding the procedure outlined in **Figure 2** (yellow box), the first step comprises building a FE mesh. For this purpose, the FE module of Simpleware software is used. The voxel FE-Grid method was chosen as it maintains the voxelized nature of the digital images, giving support to and confidence in the mesh quality.

After importing the mesh into a specific numerical program (e.g., Abaqus), it is necessary to assign each phase detected from the X-ray microtomography to a unique material with elastic properties. The pre-processing step of the numerical simulation also requires selecting the output request. The output request identifies the elements from which the simulated data will be extracted. Thus, in this case, the element output request of the middle region of the model was selected to obtain the numerical stress-strain response. **Figure 4a** provides an example of a FE mesh that displays in red the elements selected to extract the numerical responses (output elements). It should be stressed that this stage is important, as it is one of the main components of integrating the optimization technique with the Abaqus software.

The last stage of the numerical setup consists of prescribing the boundary conditions according to the experimental configuration. **Figure 4a** indicates the adopted boundary conditions chosen to represent

^f Single cell AP-608: Coretest Systems Inc., <https://coretest.com/>



the unconfined compression test performed in the laboratory. These steps characterize the pre-processing in the Abaqus software.

The final product of this step is a file (.inp in Abaqus) that contains all the necessary information to run the numerical analysis. Three MATLAB scripts were created to integrate the numerical simulations from Abaqus with the optimization technique. The first script was designed to transform the .inp file into a MATLAB format. The second script was used to execute Abaqus from the MATLAB while having the possibility of modifying the elastic parameters. The third script was designed to obtain the simulated responses from the selected output elements. **Algorithm 1** in the [Supplementary Material](#) (available online) provides a step-by-step description of how the scripts were designed to run Abaqus within a MATLAB environment.

The stages that should be performed before the inverse or surrogate modeling are outlined in this section. The next two sections describe in detail the two approaches that can be adopted.

3.3. Inverse Modeling

Inverse modeling can be understood as the process of iteratively adjusting the model parameters so that the model approximates, as closely and consistently as possible, the observed response of the system under study (48). As introduced in the previous section, this work uses Abaqus software to solve the stress – strain problem. Thus, we are interested in obtaining stress σ response at specific finite elements under specified boundary conditions (i.e., as indicated in [Fig. 4a](#)). Furthermore, the linear elastic regime is considered, as is traditionally done within the mechanical digital rock analysis framework (e.g., 2, 3). We draw further attention to this constitutive relationship described by Hooke's law and expressed in [Equation 1](#).

$$\sigma = C\varepsilon \quad (1)$$

where \mathbf{C} is the elastic matrix carrying the constitutive relationship and $\boldsymbol{\varepsilon}$ is the strain response. For the linear elastic and isotropic conditions (i.e., assuming they are appropriate for the minerals studied here), the constitutive parameters are Young's modulus, E , and Poisson ratio, ν , of each constituent material of the sample. In this paper, the constitutive relationship can be described by the contributions of a set of parameters pertaining to each solid phase (mineral) that was captured by the X-ray equipment. Assuming that $\boldsymbol{\Theta}$ is a matrix carrying the constitutive parameters of each solid phase, as expressed in **Equation 2**,

$$\boldsymbol{\Theta} = \begin{bmatrix} E_1 & \nu_1 \\ \vdots & \vdots \\ E_k & \nu_k \end{bmatrix} \quad (2)$$

where $\boldsymbol{\Theta}$ is referred to as the target parameters matrix, E_1 and ν_1 are the elastic properties of the first solid phase, and E_k and ν_k are the elastic properties of k^{th} solid phase. The goal is to merge a vector of observed, $\tilde{\sigma}$, and numerically simulated, σ_N , responses (σ_N denotes numerical) and obtain the vector or matrix of parameters $\boldsymbol{\Theta}$ that best honors the available data. This concept is summarized in **Equation 3**:

$$\tilde{\sigma} \approx \sigma_N(\boldsymbol{\Theta}) \quad (3)$$

The building blocks of this approach also require an objective function to compute the discrepancies between the model and the data, and an optimization algorithm that proposes or searches for new parameters and minimizes the objective function. In this paper, it is assumed that the residuals satisfy the Gauss theorem (48), allowing the use of the Sum of Squared Residuals (SSR) as the objective function. **Equation 4** provides the function to be minimized.

$$\text{SSR} = \sum_{i=1}^n (\tilde{\sigma}_i - \sigma_{N,i}(\boldsymbol{\Theta}))^2 \quad (4)$$

Here $\tilde{\sigma}_i$ and $\sigma_{N,i}$ denote the i^{th} observed and numerically simulated stresses out of n data points. The exploration of the parameter space of feasible solutions can be performed by any local or global optimization algorithm. Given that global search algorithms, including evolutionary approaches, are less sensitive to initial guesses and are more effective at exploring the parameter space than gradient descent methods (28), this study employs the widely used genetic algorithm (GA) (21). Genetic algorithms are widely used in computational solid mechanics for inverse analysis of material parameters (e.g., 44).

Genetic algorithms are based on evolutionary computing principles following Darwin's theory of evolution. This algorithm begins by randomly generating an initial population of solutions (i.e., $\boldsymbol{\Theta}$). The process of evolution then proceeds through the artificial processes of crossover, selection, mutation, and update of the new candidates. This process of artificial evolution (i.e., optimization) is performed for a prescribed number of generations or until an admissible error is satisfied during the evolution process.

With this brief theoretical description of the inverse modeling approach, the discussion returns to **Figure 2**. The decision indicated in the flowchart is to use the numerical setup directly linked with the parameter estimation (blue box). The stages of the GA MATLAB code are as follows:

- i. The initial population is randomly created based on specified parameter ranges.
- ii. Each set of parameters is numerically simulated
- iii. The output request is used to obtain the simulated stress-strain response, and the objective function is calculated
- iv. If the number of generations or admissible residuals is not satisfied then the evolution process takes place, a new population is proposed, and the algorithm returns to step (ii)
- v. If the termination criteria have been satisfied, then the individual, within the current population, with lowest SSR is returned to the user as optimal.

Genetic algorithms require different algorithmic parameters to run the optimization, and **Table 1** lists the settings used in this study.

To evaluate the performance of the optimal parameters four statistical performance indicators are used. These are the SSR, the coefficient of correlation (r), the coefficient of determination (R^2), and the root mean squared error (RMSE). The r is a dimensionless estimator that provides the relative correlation between measured and simulated output. The r value ranges between -1 and 1, where 1 means perfect and positive correlation. The R^2 is a dimensionless and unbiased estimator compared to r . Its value ranges from 0 to 1 with 1 meaning perfect fit. The RMSE is a popular estimator that has the dimension of the dependent variable and the advantage that large residuals receive much greater attention than small residuals. The equations of each estimator can be found in Shahin (43). The idea of using these different estimators is to evaluate the consistency of the model adjustment to the data given the optimal parameters.

Table 1: Genetic algorithm settings. This GA uses roulette wheel selection and uniform crossover.

Algorithmic parameters	Value
Population	20
Generations	100
Offspring probability	1.00
Uniform crossover gamma	0.10
Mutation rate	0.02
Mutation sigma	0.10
Selection parameter	1.00

3.4. Surrogate Model

This work uses artificial neural networks (ANN) as an optional step to link the numerical predictions with the optimization algorithm. This optional step is indicated in **Figure 2** by a green box. As outlined in the introductory section, ANN has proven to be useful for reducing the computational time associated with numerical simulations (35). Artificial neural networks can learn numerical input-output relationships, which opens new opportunities for sensitivity analysis, uncertainty quantification and parameter estimation using a large number of predictions which are quite difficult to obtain with computer-intensive models. This paper is particularly interested in the latter application. Artificial neural networks are a machine-learning technique originally proposed by McCulloch and Pitts (31). Its mathematical operations are inspired by the functioning of neurons found in the human brain.

It consists of an input layer with the independent variables, \mathbf{X} . In this work, the input matrix is composed of the linear elastic properties along with the corresponding strains. The input information of one simulation $\{E, \nu, \epsilon\}$ is compiled for several m simulations. The signal of the input layer is propagated to the fully connected neurons in the first hidden layer, which is then propagated to the following layers within the hidden part of the network. **Equation 5** summarizes the responses of each layer,

$$\mathbf{a}_j = \mathcal{F}(\mathbf{W}_j \cdot \mathbf{a}_{j-1} + \mathbf{b}_j) \quad (5)$$

where \mathbf{a}_j is the output response of an arbitrary j^{th} hidden layer, \mathbf{W}_j is the corresponding weights matrix, \mathbf{a}_{j-1} is the response of the previous layer, which assumes $\mathbf{a}_{j-1} = \mathbf{X}$ if it is the input layer, \mathbf{b}_j is the bias vector of the current layer, and \mathcal{F} is a user-defined activation function. When \mathbf{a}_j reaches the output layer no activation function is used, and the surrogate stress responses are obtained as indicated by **Equation 6**,

$$\sigma_s = \mathbf{a}_j \quad (6)$$

where σ_s is the surrogate model stress response (σ_s denotes surrogate). Ultimately the surrogate model should be capable of predicting the numerical model responses with a sufficient degree of accuracy to replace the numerical solution, that is, $\sigma_s = \sigma_N$.

In this paper, a total of $m = 100$ simulations were conducted to compose the numerical database. The effects of sample size require further investigation, yet this number is considered for computational cost convenience. The constitutive properties are drawn from uniform distribution and are selected so that the surrogate model does not extrapolate the training and testing data when performing the optimization via GA. The simulations used to compose the database were performed with three data points each $\epsilon = \{\epsilon_1, \epsilon_2, \epsilon_3\}$. A total number of 300 data points were generated, of which 210 were data points (70%) used for training the network and 90 were data points used for testing the network on

unseen data (30%). The Regression Neural Network package, available at MATLAB, was used to train the networks and **Table 2** indicates the ANN adopted settings. The hyperparameters were selected using a random search strategy (6) across 40 different configurations. The number of neurons, layers and transfer functions were also drawn from uniform distribution using the values indicated in **Table 2**. Three activation functions were considered, and they were indexed to convey the random creation of network configurations.

Table 2: Artificial Neural Network settings.

Algorithmic parameters	Value
Data division	Random
Number of configurations	40
Number of neurons	(1, 2, ... , 5)
Number of layers	(1, 2, ... , 10)
Activation function 1	ReLu
Activation function 2	Tanh
Activation function 3	Sigmoid
Learning algorithm	LBFGS
Epochs	1000
<i>ReLu = Rectified linear unit; Tanh = Hyperbolic tangent; LBFGS = Broyden-Fletcher-Goldfarb-Shanno quasi-Newton algorithm.</i>	

The selection of a representative ANN structure is based on the performance of both training (calibration) and testing (unseen) datasets. The model structure that has the highest R^2 and lowest RMSE for training and testing datasets, and presents the lowest discrepancy between both datasets, is chosen. This procedure aims to select the best-performing structure that favors predictability and avoids overfitting (22). The surrogate model is then used as the prediction tool in the parameter estimation stage as previously discussed in Section 3.3. Note that using ANN for the adopted modeling conditions is simple, yet the methodology can be easily adapted for more complex nonlinear conditions, where capturing physical responses becomes challenging. The methodology is thus useful to inform scholars about

an alternative solution for the computational burden associated with the numerical forward run. We point out that the successful application of the methodology for simpler conditions as shown herein is promising for future nonlinear stress-strain applications.

3.5. Case Studies

Two case studies were used to evaluate the methodology: one based on a synthetic single-solid-phase model, and another based on a real-world multi-solid-phase model, as shown in **Figure 4b** and **c**.

Synthetic-generated data composes the first case study. This case was used to validate the methodology, and the simulations were conducted with a single solid phase as illustrated in **Figure 4b**. The single-phase corresponds to Grain 0 (in gray color) which has a prescribed Young's modulus of 40 GPa and a Poisson ratio of 0.08. These prescribed properties are not related to any mineral as they are used only to validate the algorithm. Nevertheless, their values were selected to fairly agree with values of minerals that are used for mechanical simulations using DRA. To further validate the methodology, the synthetic stress-strain response (i.e., numerical created) was used as the "observed evidence". To obtain the data, an unconfined compression simulation was first performed, and the numerical stress-strain response was recorded. The numerical stress and strain curve then serve as the observed data for the optimization process. The underlying idea of this case study is to recover the ground true value of the Young's modulus, which is known.

The real-world data obtained by the unconfined compression test composes the second case study. For this condition three solid phases, as indicated in **Figure 4c**, were identified. Grain 1 (blue color) comprises the main grains identified by the light gray color in the gray-scale

Table 3: Considered parameters and search range for the two scenarios. Young's modulus, E , is in GPa and Poisson ratio, ν , is unitless. ^f represents the fixed parameters, and values in brackets () constrain the search-space.

Phase	Synthetic case		Real-world case	
	E	ν	E	ν
Grain 0	(10 - 70)	0.08 ^f	-	-
Grain 1	-	-	(20 - 110)	0.08 ^f
Grain 2	-	-	(10 - 120)	0.08 ^f
Cement	-	-	(0.5 - 50)	0.08 ^f
Pore	0 ^f	0 ^f	0 ^f	0 ^f

images, Grain 2 (yellow color) indicates the smaller grains mapped in white color in the gray-scale images, while the Cement (cyan color) represents the material surrounding the main grains and is identified by the dark gray color in the gray-scale images obtained by the scanning equipment. X-ray powder diffraction (XRD), X-ray fluorescence analysis (XRF), and thin section analysis, were performed to help delineate the range of the parameters. While XRD identifies the crystalline phases present, XRF quantifies the total elemental composition of the samples. These analyses, which will be further explored in the Results section, revealed the presence of quartz, pyrite, and clay minerals while also indicating intricate “imperfections” of the main grains. Such information was associated with the content found in the X-ray microtomography images and helped to formulate [Table 3](#). Quartz, pyrite, and clay minerals were assigned to Grain 1, Grain 2, and Cement, respectively. The adopted linear elastic range of values was supported by information provided by Ändra et al. (2) and Schön (41). Note from [Table 3](#) that there is a particular interest in estimating Young’s modulus values from the stress-strain relationship and that the Poisson ratio is fixed to the values of intact minerals.

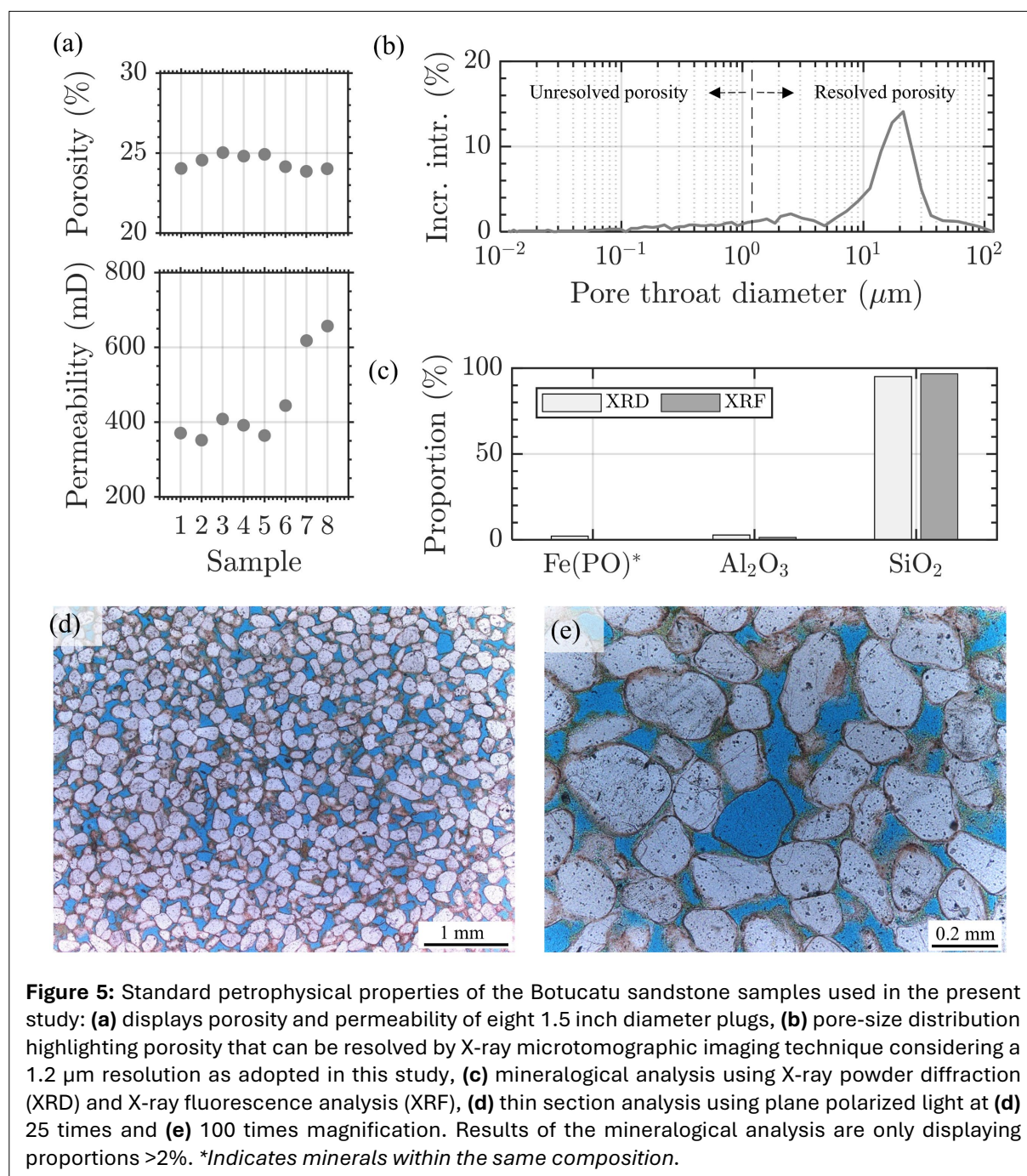


Figure 5: Standard petrophysical properties of the Botucatu sandstone samples used in the present study: **(a)** displays porosity and permeability of eight 1.5 inch diameter plugs, **(b)** pore-size distribution highlighting porosity that can be resolved by X-ray microtomographic imaging technique considering a 1.2 μm resolution as adopted in this study, **(c)** mineralogical analysis using X-ray powder diffraction (XRD) and X-ray fluorescence analysis (XRF), **(d)** thin section analysis using plane polarized light at **(d)** 25 times and **(e)** 100 times magnification. Results of the mineralogical analysis are only displaying proportions >2%. *Indicates minerals within the same composition.

4. RESULTS

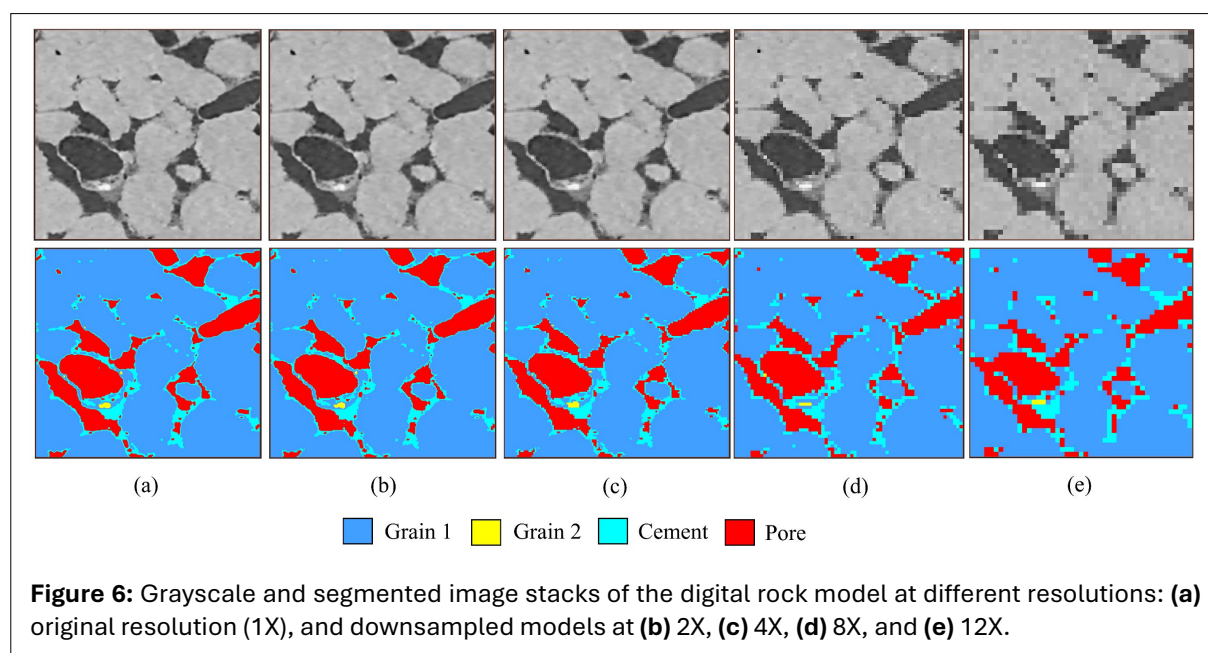
This section is organized into four subsections. The first subsection introduces laboratory data for the Botucatu sandstone, which serve as reference properties for the DRA. The second subsection examines the downsampled models to identify a configuration that balances representative digital properties with computational efficiency. The third and fourth subsections present the parameter estimation results for the synthetic and real-world cases, using the numerical and surrogate models, respectively.

4.1. Laboratory Characterization

Standard properties of the Botucatu sandstone used in this study are presented in [Figure 5](#). Porosity and Permeability of eight rock plugs are shown in [Figure 5a](#). As observed in other studies (e.g., [7](#)), the graph indicates that the porosity values of this rock do not have an expressive variation. Permeability values, on the other hand, indicate a more remarkable variation amongst the samples. With respect to the pore-size distribution as indicated in [Figure 5b](#), the Botucatu sandstone has a mono-modal distribution. This piece of information is key to show that most pores are around 20 μm . [Figure 5b](#) thus indicates, given the sample characteristics, that the adopted 1.2 μm resolution is sufficient to resolve the pore space using X-ray microtomographic equipment settings. [Figure 5c](#) highlights that the main mineralogical composition consists of quartz (SiO_2), supported by the presence of intense peaks at characteristic 2θ angles ([Fig. A2](#) in the [Supplementary Material](#), available online). This information agrees with previous studies using this rock type. [Figure 5d](#) and [e](#) present thin section analysis indicating a homogeneous grain and pore size network. [Figure 5e](#) provides a closer look at the main grain, and the 2D images highlight the intricate imperfections of the main grain (a piece of information that suggests the potential variations of the linear elastic properties of the minerals contained in this rock). The readers are now informed about the petrophysical characteristics of the samples used in this study. Geological characteristics of the formation are not in the scope of this paper and interested readers are referred to Schere and Lavina ([39](#)) for a comprehensive geological description.

4.2. Downsampled Models

[Figure 6a–e](#) presents the grayscale and segmented images of the original 1X and downsampled 2X, 4X, 8X, and 12X models, respectively. These images, in particular the segmented representation, provide good evidence that the pore and solid structures may maintain their original structure with small downsampling. This information can be seen in [Figure 6a, b, and c](#). Larger downsamplings may produce a slight or a relatively large loss of information. For instance, the pore-structure of the original model, available in [Figure 6a](#), and the largest downsampled model, presented in [Figure 6e](#), indicates the loss of small pores and connection/disconnection of other pore-structures. Although only one stack is



evaluated, this impact is assumed to influence the entire domain. This impact is further quantified in terms of petrophysical properties.

The digital petrophysical results are based on the five downsampled scenarios. The porosities were calculated by dividing the segmented pore domain by the sum of the solid and pore domains, as described in Section 3.1. Both the total and the connected portions had negligible differences, therefore only the connected porosity is shown in Figure 7.

Figure 7a shows the porosity results. The mean laboratory porosity corresponds to 24.42% (solid gray line) and the minimum and maximum laboratory values are 23.86 and 25.03%, respectively (shaded gray region). A discrepancy of up to 10% of the laboratory minimum and maximum values (dashed gray line) is herein considered reasonable to compare the porosity values from these two techniques. The graph indicates that the digital porosity has negligible differences amongst the downsampled models. These values are also within 10% of admissible errors. The results, therefore, indicate good agreement between the porosities obtained in both laboratory and DRA. Additionally, downsampling shows no effect on the digital porosity.

The permeability results are displayed in Figure 7b. The mean laboratory permeability is 450 mD (solid gray line), while minimum and maximum values are 352 and 657 mD (gray-shaded region), respectively. A 10% discrepancy (gray dashed line) is also considered for the permeability analysis. The digital models indicate a reduction of the permeability while increasing the downsampling. The original model (1X) yields a permeability of 526 mD, which is in good agreement with the laboratory measurements. Model 2X, with a value of 435 mD, also falls within the laboratory bounds. Models 4X and 8X, with permeabilities of 336 and 342 mD, respectively, lie within the acceptable 10% discrepancy range. The 12X model is marginally outside the 10% discrepancy threshold. Overall, downsampling has a greater impact on digital permeability. The permeability decreases as the downsampling factor increases, suggesting that pore-structure disconnection becomes significant at higher levels of downsampling.

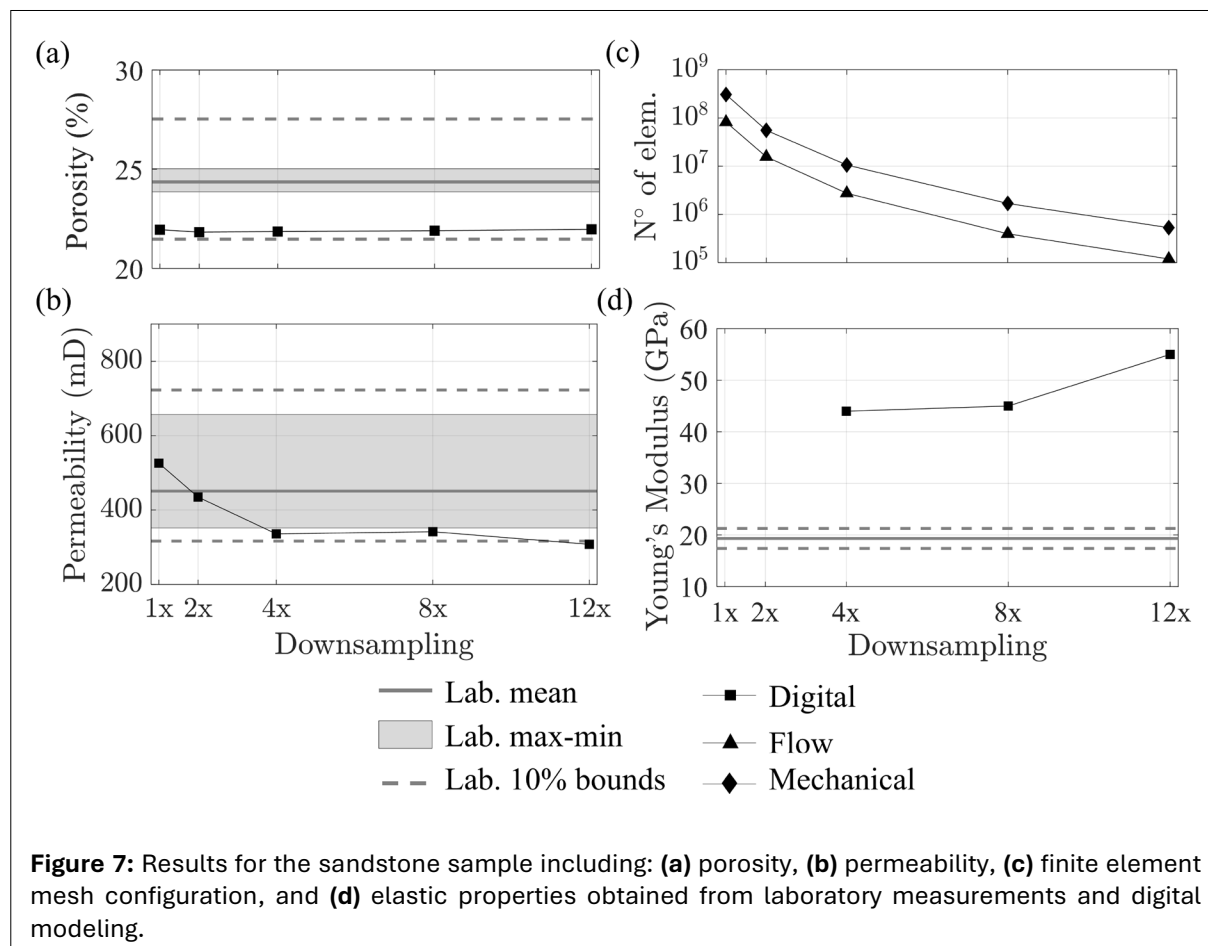


Figure 7c presents the number of finite elements for each downsampled model, highlighting that fluid-flow simulations are less computationally demanding as they rely on the pore phase only. As shown in **Figure 7d**, only the coarser models (i.e., 4X, 8X, and 12X) were simulated in Abaqus, since finer discretizations exceeded the available computational memory. These simulations, which adopted elastic parameters of $E = 94$ GPa and $\nu = 0.08$, revealed that coarser discretizations led to an apparent increase in stiffness, yielding higher estimated rock Young's modulus than that measured in laboratory test. Despite these constraints, the 8X downsampled model is representative in terms of porosity and permeability, as its values fall within the permitted 10% discrepancy. It also has a similar number of finite elements as the 12X model, and mechanical properties comparable to the 4X model. Therefore, the 8X model was selected to conduct the inversion procedure.

4.3. Elastic Properties: Inverse Modeling

This subsection presents the results of the two case studies using the inverse modeling approach. The synthetic case is discussed first, followed by the real-world case.

The synthetic case was specifically designed to test the proposed methodology as the ground true parameter of Grain 0 is known ($E = 40$ GPa). **Figure 8a** provides the graphical adjustment of both datasets using the stress-strain relationship. This graph indicates a nice fit among the datasets. The strong agreement can be attributed to the fact that the numerical response is a perfect representation of the synthetically created data, which plays the role of the "observed" evidence. **Table 4** provides the estimated E via inverse modeling. As can be seen, in the second column of the table, the model represents, with adequate accuracy, the ground true E value. **Table 5** provides the adjustment statistics for the first case study. As expected from the results presented in **Table 4**, the four adjustment statistics indicate a nice fit between observed and simulated datasets. Note that the order of SSR and RMSE are low given the range of values of the dependent variable (0 – 60 MPa). In addition, the dimensionless metrics (R^2 and r) provide adequate values.

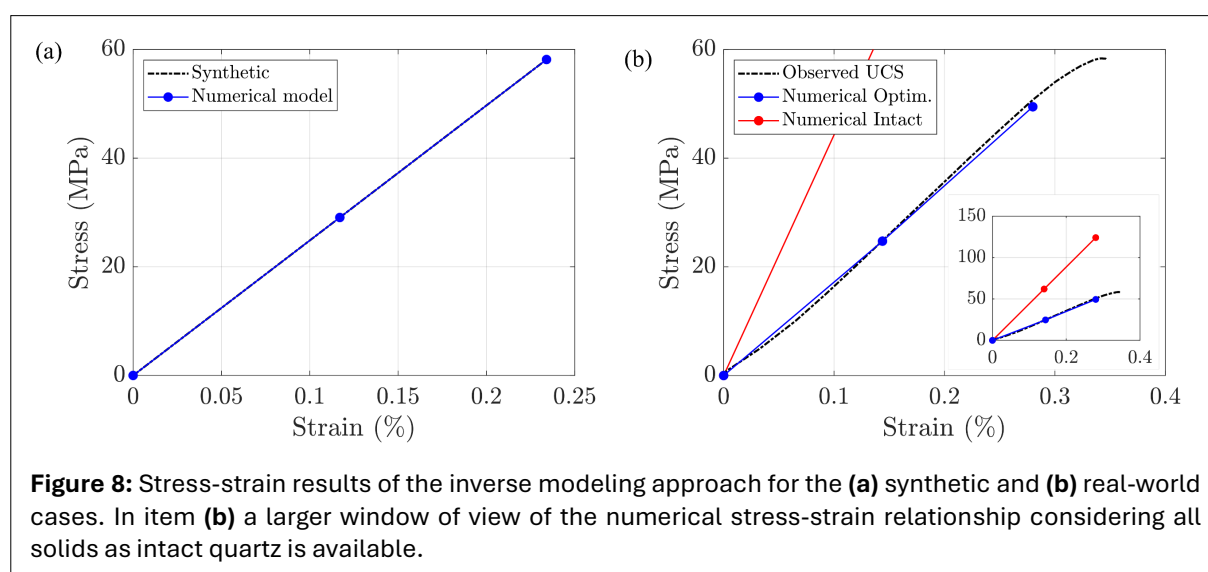
The real-world case is now presented to assess the potential of the methodology when applied to real rocks and laboratory test data. **Figure 8b** provides the graphical adjustment of both datasets using the

Table 4: Estimated parameters via inverse modeling approach.

Solid phase	Estimated E (GPa)	
	Synthetic case	Real-world case
Grain 0	40.0003	-
Grain 1	-	43.1171
Grain 2	-	90.6090
Cement	-	15.4032

Table 5: Adjustment statistics for the inverse modeling approach.

Statistical Metric	Synthetic case	Real-world case
SSR (MPa) ²	$9.68 \cdot 10^{-10}$	0.386
R^2	0.999	0.999
r	0.999	0.999
RMSE (MPa)	$0.22 \cdot 10^{-4}$	0.439



stress-strain relationship. Note from this graph that, within the linear regime, the observed data and the simulation using the optimal parameters exhibit an excellent fit. Furthermore, for comparative purposes, simulation using values of intact minerals is provided. The three solid phases are represented by quartz, using the elastic values provided by Schön (41) ($E = 94$ GPa and $\nu = 0.08$). This simulation indicates a significant overestimation relative to the observed values and reinforces the need for calibration procedures, as proposed in this paper. Additionally, the simulations are limited to the linear regime, suggesting that additional effort is needed to represent the nonlinear behavior of the curve, such as crystal plasticity effects. Table 4 provides the estimated parameters for the three solid phases (Grain 1, Grain 2, and Cement). The main solid phase, Grain 1, represents 86.4% of the solid bulk and its value (43 GPa) is approximately half of Young's modulus of the intact quartz mineral. Such a finding highlights the alteration/variability of the quartz mineral within this sample. The cement represents 13.5% of the solid bulk and its value (15 GPa) indicates a higher degree of alteration compared to the main grain (Grain 1). Notably, the material in contact with the pore spaces—herein referred to as Cement—is more susceptible to numerous physical and chemical processes that may accelerate its alteration and consequently weaken the material. The minor bright grains (Grain 2) represent 0.1% of the solid bulk. The estimated value for this solid phase (91 GPa) indicates a stronger material if compared to the previous ones. These findings are also in agreement with the insights given by X-ray microtomographic images. As presented in Figure 6a, the darker material (Cement) is less dense than the light-gray material (Grain 1) and the white material (Grain 2). Therefore, it should be expected that the Cement would represent the soft material, whereas Grain 2 would represent the stiff material. Additionally, the imperfections of the main grains (intra-particle porosity and fractures) as seen in Figure 5e may be further evidence that modeling elastic properties of sandstone rocks using intact quartz values might not be an appropriate assumption.

The RMSE values indicated in Table 5 highlight larger residual values for the real-world case. This occurs because reproducing real laboratory experiments is significantly more challenging than working with synthetic observations, where all controlling factors (such as constitutive properties and boundary conditions) are fully known. Despite residual differences, the adjustment shown in Figure 8b suggests that the assumptions considered in this work are sufficient.

In this work, we follow the assumption that the Poisson ratio is a fixed property and assumes the value of intact quartz ($\nu = 0.08$). Therefore, throughout the optimization process, its value remains as a permanent scalar. To further evaluate the effect of this assumption, the observed radial strains obtained by the uniaxial compression strength (UCS) and the numerically simulated radial strains are presented in Figure 9. The numerically simulated radial strains were computed from contributions of both the x and y directions of the model. From the curves, it is noticeable that for the same radial strains, the reached stresses are far lower when using the model with adjusted parameters (blue curve) if compared to the intact parameters (red curve). Nevertheless, we recognize that further improvements may be achieved if the Poisson ratio is to be included as an unknown property.

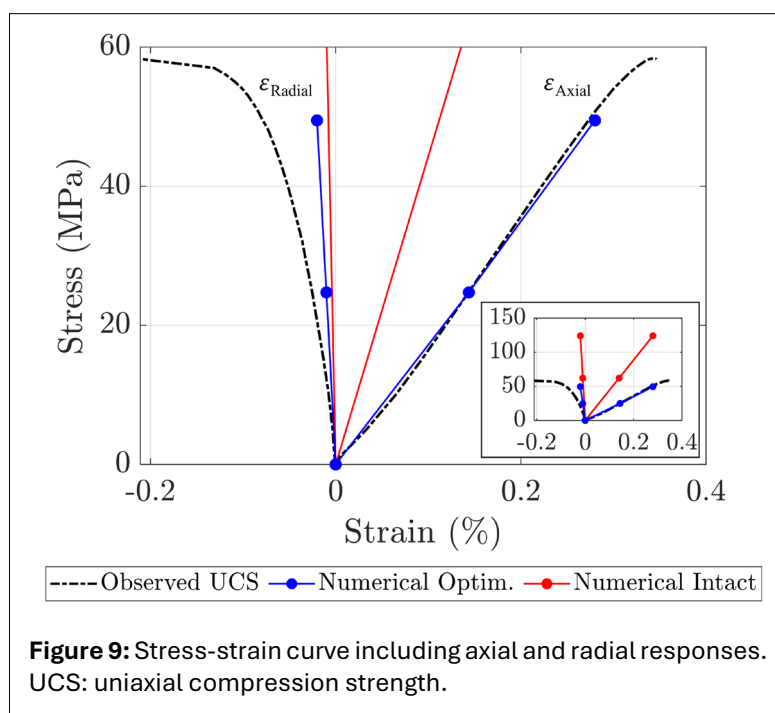


Figure 9: Stress-strain curve including axial and radial responses. UCS: uniaxial compression strength.

4.4. Elastic Properties: Surrogate Model

This subsection presents the results of two case studies using the surrogate model as a prediction tool. First, the performance of the selected model is presented. Then, the parameter estimation results obtained using the ANN models as predictors are discussed.

For the first case study, the selected model consisted of one hidden layer with 10 neurons and employed the ReLU activation function. The ANN model achieved an R^2 of 0.999 and an RMSE of 1.61×10^{-5} MPa for the training group (calibration), and an R^2 of 0.999 and an RMSE of 1.68×10^{-5} MPa for the testing group (performance on unseen data), indicating adequate performance and demonstrating the robustness of the model. **Figure 10a** shows the agreement between the numerical database and the ANN predictions for both the training and testing groups, highlighting in the 1:1 space the strong fit of the surrogate model in reproducing the numerical responses. Overall, for the single-solid phase, good calibration was achieved particularly because of a high R^2 and a low RMSE. **Figure 11a** presents the stress-strain responses using the optimized elastic property. The figure indicates overlapping between observed and predicted (via surrogate model) stress-strain. **Table 6** confirms that the “known” parameter was adequately recovered (i.e., Grain 0 value) using the surrogate modeling and GA optimization. **Table 7** indicates similar adjustment statistics as in the inverse modeling case (**Table 5**). Note that although the surrogate provides a slightly better recovery of the imposed parameter, the residuals are larger when using the ANN. This could be explained by the fact that the ANN structure is not a perfect representation of the numerical tool. Such imperfection is reflected in slightly higher SSR and RMSE (although negligible from a practical point of view).

Table 6: Estimated parameters using the surrogate model as predictive tool.

Solid phase	Estimated E (GPa)	
	Synthetic case	Real-world case
Grain 0	40.0001	-
Grain 1	-	46.8661
Grain 2	-	112.2142
Cement	-	12.0667

representation of the surrogate model. Compared to the single-solid phase case, the multi-solid phase ANN predicts the numerical responses with greater difficulty due to the inclusion of additional parameters associated with the different phases. Nevertheless, the graphs indicate that the surrogate model provides a good representation of the numerical model, as the points fall close to the 1:1 line. The adjustment statistics, characterized by consistently high R^2 and low RMSE values, provide further evidence that the surrogate model can effectively replace the numerical analysis. **Figure 11b** presents

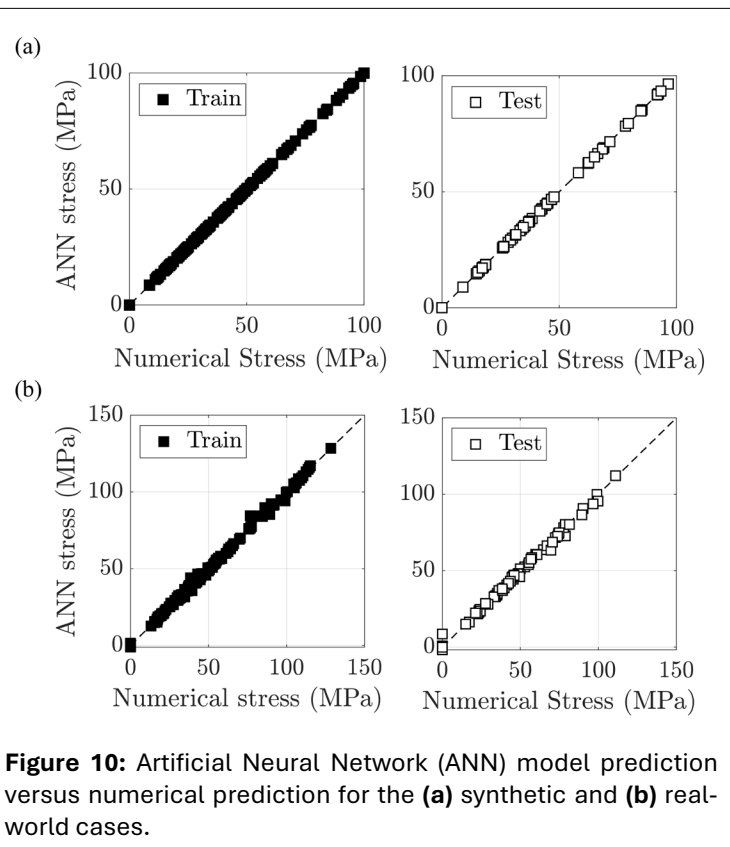
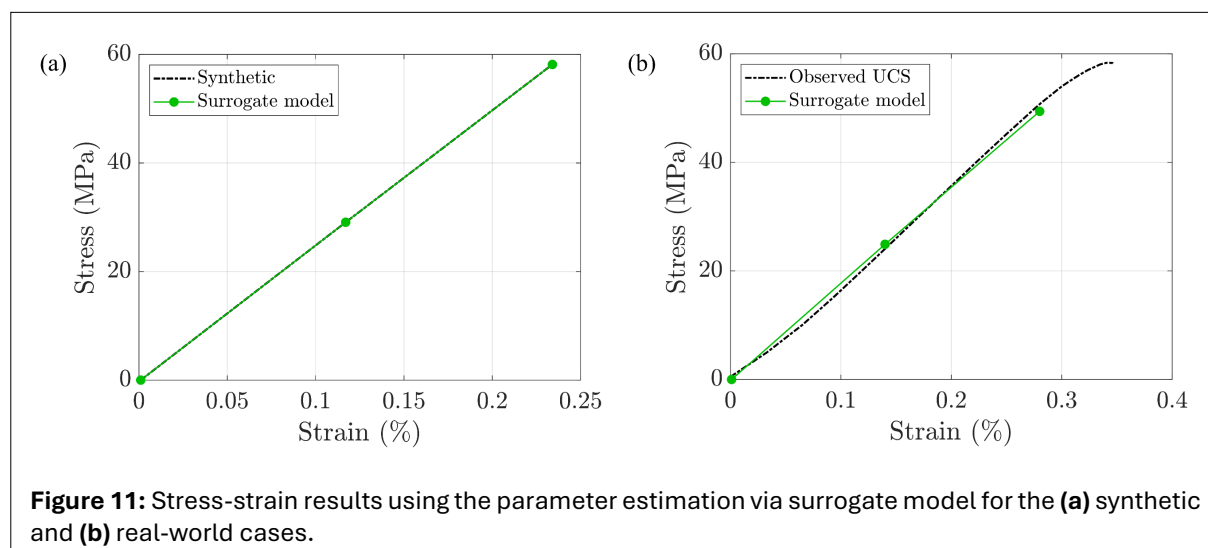


Figure 10: Artificial Neural Network (ANN) model prediction versus numerical prediction for the (a) synthetic and (b) real-world cases.

For the second case study, the selected model comprised one hidden layer with 7 neurons and used the ReLU activation function. The ANN model achieved an R^2 of 0.999 and an RMSE of 1.237 MPa for the training group, and an R^2 of 0.997 and an RMSE of 1.642 MPa for the testing group. These performance indicators, characterized by high R^2 and low RMSE values, demonstrate the robustness of the surrogate model for this case. **Figure 11b** shows the agreement between the numerical database and the ANN predictions, illustrating in graphical format the adequate and unbiased



the surrogate responses with optimized properties. The graph indicates the good fit between the observed and predicted (via surrogate model) stress-strain. **Table 6** presents the estimated parameters for Grain 1, Grain 2, and Cement. Their values are similar to those found by the inverse modeling with differences of 3.7 GPa for Grain 1, 21.6 GPa for Grain 2, and 3.0 GPa for the Cement. Grain 2 showed the largest difference in the estimated values, and its contribution to the bulk property warrants further investigation. Grain 2 represents a minor contribution to the rock, and it may also assume different values

Table 7: Adjustment statistics when using the surrogate model as predictive tool.

Statistical Metric	Synthetic case	Real-world case
SSR (MPa) ²	$9.38 \cdot 10^{-9}$	0.416
R ²	0.999	0.999
r	0.999	0.999
RMSE (MPa)	$0.68 \cdot 10^{-4}$	0.456

without compromising the predicted response. Further investigation is required to understand the sensitivity of Grain 2, as well as that of the other materials. **Table 7** indicates similar adjustment statistics as in the inverse modeling case (**Table 5**).

Table 8 presents the computational time for both inverse and surrogate modeling. It was found that, given the hardware used, the inverse modelling approach—when combined with a downsampling

procedure—requires approximately 10 days of interruptive calculations. The surrogate modeling, on the other hand, requires far fewer computation resources. In fact, the most computationally intensive task is constructing the database used to train the ANN structures, which requires approximately 9.6 hours under the settings adopted in this paper. In this study, 2000 simulations were used in inverse modeling and 100 numerical simulations in the surrogate model, which justifies a lower computational cost. The surrogate modeling requires far lower computational resources to train the ANNs and to estimate the parameters using GA, compared to the inverse modeling. For example, the first case study required 41.61 seconds for training the various network configurations, and 101.22 seconds for the subsequent parameter estimation. These findings are promising, as they open new opportunities to use state-of-the-art optimization algorithms that require a large number of predictions to adequately explore the parameter search space.

5. CONCLUSIONS

This work presents a protocol for estimating the elastic properties of minerals using X-ray computed microtomography, inverse modeling, and a surrogate model. Two case studies were designed to validate and evaluate this approach using

Table 8: Computational time for the two approaches using an Intel(R) Core (TM) i9-7920X CPU @ 2.90GHz and 128 GB of RAM machine.

Approach	Procedure	Computational time (days)
Inverse modeling	Parameter estimation	10.0
Surrogate model	Database creation	0.4
	ANN calibration	0.0005
	Parameter estimation	0.0012

synthetic data (created numerically) and real-world data (laboratory measurements). Overall, the results of these case studies are promising, as the parameters estimated through inverse modelling are consistent with those obtained from laboratory experiments in the real case, as well as with the X-ray microtomographic observations, in which stiffer materials appear as brighter (denser) phases in the digital images. Additionally, the adjusted response for the real case shows a significant improvement relative to simulations assuming intact mineral properties. Four statistical indicators support the good agreement between observed and simulated datasets, confirming the overall effectiveness of the implementation.

Using a surrogate in this context to overcome the high computational cost associated with the forward numerical simulation is promising. Artificial Neural Networks have been shown to be useful for this task as they capture with a good degree of accuracy the responses of the numerical simulations and can thus replace numerical schemes. The surrogate methodology presented in this paper can be easily applied to more complicated responses, including non-linear regime with the possible addition of recurrent networks. Overall, the computational cost associated with surrogate modeling lies primarily in building the database, which—as demonstrated in this study—is far smaller than the number of simulations required for the inverse modeling approach using a global optimization algorithm.

Despite the efforts made to address and present this research, there are several implications and opportunities that extend beyond the case studies examined here. The proposed framework, while focusing on a sandstone sample, could also be applied to a wide variety of rocks with complex pore networks. While considered a fixed property, the Poisson ratio can be included as an unknown parameter. An improved understanding of the correlation between more than one solid phase is still required for the optimization portion. Extending this methodology to the non-linear regime is a step forward toward the incorporation of micromechanisms observed in rock deformation. Finally, to support a fair and open scientific discussion, additional sources of discrepancies between simulated and observed data—beyond those hypothesized in this paper—should be investigated.

STATEMENTS AND DECLARATIONS

Supplementary Material

An Appendix to this paper is available for downloading [here](#).

Acknowledgements

The material presented in this paper is part of a project sponsored by Equinor Brazil using funds made available by the RD&I Clause of the contracts for oil and gas exploration in Brazil. The authors would like to express thanks to Equinor for allowing the publication of these results. The Brazilian National Petroleum Agency (ANP) is responsible for analyzing, approving, monitoring, and supervising the investment of funds arising from the RD&I Clause.

Author Contributions

Ruan Gomes: conceptualization, methodology, software, interpretation, original draft. **Sergio Fontoura:** conceptualization, validation, supervision, manuscript editing. **Guilherme Righetto:** validation, software, data acquisition, manuscript editing. **Luiza Fernandes** and **Rafael Lopez:** data acquisition, manuscript editing. **Rafaella Sampaio, Claudio Lima, Marcel Naumann,** and **William Silva:** manuscript editing.










Conflicts of Interest

The authors declare that they have no known competing financial interests or personal relationships that could have appeared to influence the work reported in this paper.

Data, Code & Protocol Availability

All data that supports the findings of this study are available from the corresponding author upon reasonable request.

ORCID IDs

Ruan Gomes	 https://orcid.org/0000-0002-1376-0995
Sergio Fontoura	 https://orcid.org/0000-0003-0493-4567
Guilherme Righetto	 https://orcid.org/0009-0007-9048-1600
Luiza Fernandes	 https://orcid.org/0009-0003-4565-0517
Rafael Lopez	 https://orcid.org/0009-0006-6251-6266
Rafaella Sampaio	 https://orcid.org/0009-0009-4314-3726
Claudio Lima	 https://orcid.org/0009-0004-9003-1843
Marcel Naumann	 https://orcid.org/0000-0002-9885-4295
William Silva	 https://orcid.org/0000-0003-1879-9386

REFERENCES

1. Abaqus (2014) Analysis User's Manual, Version 6.14, Dassault Systems Simulia, Inc. <https://www.scribd.com/document/517828704/Analysis-4>
2. Andrä H, Combaret N, Dvorkin J, et al. (2013). Digital rock physics benchmarks - part II: Computing effective properties. *Computer & Geosciences* 50, 33–43. <https://doi.org/10.1016/j.cageo.2012.09.008>
3. Arns C, Knackstedt M, Pinczewski W, Garboczi E. (2002). Computation of linear elastic properties from microtomographic images: Methodology and agreement between theory and experiment. *Geophysics* 67, 1396–1405. <https://doi.org/10.1190/1.1512785>
4. Asher M, Croke B, Jakeman A, Peeters L. (2015). A review of surrogate models and their application to groundwater modeling. *Water Resources Research* 51, 5957–5973. <https://doi.org/10.1002/2015WR016967>
5. Bear J. (1972). Dynamics of Fluids in Porous Media. Dover Publications INC, New York, 800 pgs.
6. Bergstra J, Bengio Y. (2012). Random Search for Hyper-Parameter Optimization. *Journal of Machine Learning Research* 13, 281–305.
7. Cardoso O, Balaban R. (2015). Comparative study between Botucatu and Berea sandstone properties. *Journal of South American Earth Sciences* 62, 58–69. <https://doi.org/10.1016/j.jsames.2015.04.004>
8. Cartwright-Taylor A, Main I, Butler I, et al. (2020). Catastrophic failure: How and when? Insights from 4-D in situ x-ray microtomography. *JGR Solid Earth* 125, 8, e2020JB019642. <https://doi.org/10.1029/2020JB019642>
9. Cnudde V, Boone M. (2013). High-resolution X-ray computed tomography in geosciences: A review of the current technology and applications. *Earth-Science Reviews* 123, 1–17. <https://doi.org/10.1016/j.earscirev.2013.04.003>
10. Dong H, Blunt M. (2009). Pore-network extraction from micro-computerized-tomography images. *Physical Review E* 80, 036307. <https://doi.org/10.1103/PhysRevE.80.036307>
11. Ettermeier F, Lechner P, Hofmann T, Andrä H, Schneider M, et al. (2019). Digital Sand Core Physics: Predicting physical properties of sand cores by simulations on digital microstructures. *International Journal of Solids and Structures* 188–189, 155–168. <https://doi.org/10.1016/j.ijsolstr.2019.09.014>
12. Faisal T, Awedalkarim A, Chevalier S, Jouini M, Sassi M. (2017). Direct scale comparison of numerical linear elastic moduli with acoustic experiments for carbonate rock X-ray CT scanned at multi-resolutions. *Journal of Petroleum Science and Engineering* 152, 653–663. <https://doi.org/10.1016/j.petrol.2017.01.025>
13. Faisal T, Islam A, Jouini M, Devarapalli R, Jouiad M, et al. (2019). Numerical prediction of carbonate elastic properties based on multi-scale imaging. *Geomechanics for Energy and the Environment* 20, 100125. <https://doi.org/10.1016/j.gete.2019.100125>
14. Ferreira L, Surmas R, Tonietto S, da Silva M, Peçanha R. (2020a). Modeling reactive flow on carbonates with realistic porosity and permeability fields. *Advances in Water Resources* 139, 103564. <https://doi.org/10.1016/j.advwatres.2020.103564>
15. Ferreira T, Rasband W. (2012). ImageJ user guide - IJ 1.46.r, National Institute of Health Bethesda, MD. <https://imagej.net/ij/docs/guide/>
16. Ferreira LP, Oliveira T, Surmas R, Silva M, Peçanha R. (2020b). Brinkman equation in reactive flow: Contribution of each term in carbonate acidification simulations. *Advances in Water Resources* 144, 103696. <https://doi.org/10.1016/j.advwatres.2020.103696>
17. Fu J, Thomas H, Li C. (2021). Tortuosity of porous media: Image analysis and physical simulation. *Earth-Science Reviews* 212, 103439. <https://doi.org/10.1016/j.earscirev.2020.103439>
18. Furtney J, Thielens C, Le Goc R. (2022). Surrogate models in rock and soil mechanics: Integrating numerical modeling and machine learning. *Rock Mechanics and Rock Engineering* 55, 2845–2859. <https://doi.org/10.1007/s00603-021-02720-8>

19. Gerke K, Vasilyev RV, Khirevich S, et al. (2018). Finite-difference method Stokes solver (FDMSS) for 3D pore geometries: Software development, validation and case studies. *Computers and Geosciences* 114, 41–58. <https://doi.org/10.1016/j.cageo.2018.01.005>
20. Gerke K, Sizonenko TO, Karsanina M, Lavrukhin EV, Abashkin V, et al. (2020). Improving watershed-based pore-network extraction method using maximum inscribed ball pore-body positioning. *Advances in Water Resources*, 140, 103576. <https://doi.org/10.1016/j.advwatres.2020.103576>
21. David E. Goldberg. (1989). Genetic Algorithms in Search, Optimization and Machine Learning (1st. ed.). Addison-Wesley Longman Publishing Co., Inc., USA. <https://dl.acm.org/doi/10.5555/534133>
22. Gomes R, Gomes G, Vrugt J. (2022). A hybrid multi-step sensitivity-driven evolutionary polynomial regression enables robust model structure selection. *Engineering Application of Artificial Intelligence* 116, 105421. <https://doi.org/10.1016/j.engappai.2022.105421>
23. Gostick J. (2017). Versatile and efficient pore network extraction method using marker-based watershed segmentation. *Physical Review E* 96, 023307. <https://doi.org/10.1103/PhysRevE.96.023307>
24. Hernández-Pico R, Fontoura S, Righetto G, et al. (2014). Mechanical tests on digital samples of carbonates obtained using X-Ray microtomography, SBMR, VI Rock Mechanics Symposium, Goiania, Brazil.
25. Hussain M, Javadi A, Ahandar-Asr A, Farmani R. (2015). A surrogate model for simulation-optimization of aquifer systems subjected to seawater intrusion. *Journal of Hydrology* 523, 542–554. <https://doi.org/10.1016/j.jhydrol.2015.01.079>
26. Kim K, Zhuang L, Yang H, Kim H, Min K. (2015). Strength anisotropy of Berea sandstones: Results of X-Ray computed tomography, compression tests, and discrete modeling. *Rock Mechanics and Rock Engineering* 49, 1201–1210. <https://doi.org/10.1007/s00603-015-0820-0>
27. Lucas-Oliveira E, Araujo-Ferreira A, Trevizan W, dos Santos B, Bonagamba T. (2020). Sandstone surface relaxivity determined by NMR T2 distribution and digital rock simulation for permeability evaluation. *Journal of Petroleum Science and Engineering* 193, 107400. <https://doi.org/10.1016/j.petrol.2020.107400>
28. Marquardt D. (1963). An algorithm for least-squares estimation of nonlinear parameters. *Journal of the Society for Industrial and Applied Mathematics* 11, 2, 431–441. <https://doi.org/10.1137/0111030>
29. McBeck J, Aiken J, Ben-Zion Y, Renard F. (2020). Predicting the proximity to macroscopic failure using local strain populations from dynamic in situ X-ray tomography triaxial compression experiments on rocks. *Earth and Planetary Science Letters* 543, 116344. <https://doi.org/10.1016/j.epsl.2020.116344>
30. McBeck J, Kandula N, Aiken J, et al. (2019). Isolating the factors that govern fracture development in rocks throughout dynamic in situ X-Ray tomography experiments. *Geophysical Research Letters* 46, 20, 11127–11135. <https://doi.org/10.1029/2019GL084613>
31. McCulloch W, Pitts W. (1943). A logical calculus of the ideas immanent in nervous activity. *The Bulletin of Mathematical Biology* 5, 115–133
32. Montanheiro T, Artur A, Montanheiro F, Negri F, Gesicki A, et al. (2011). Investigação tecnológica de arenitos silicificados da formação Botucatu (NE do Paraná) para uso como rochas de revestimento [Technological investigation of silicified sandstones from the Botucatu Formation (NE Paraná) for use as cladding stone]. *Geociências* 30, 2, 237–251.
33. Narsilio G, Buzzi O, Fityus S, Yun T, Smith D. (2009). Upscaling of Navier-Stokes equation in porous media: Theoretical, numerical and experimental approach. *Computer and Geotechnics* 36, 7, 1200–1206. <https://doi.org/10.1016/j.compgeo.2009.05.006>
34. Njock P, Shen S, Zhou A, Modoni G. (2021). Artificial neural network optimized by differential evolution for predicting diameters of jet grouted columns. *Journal of Rock Mechanics and Geotechnical Engineering* 13, 6, 1500–1512. <https://doi.org/10.1016/j.jrmge.2021.05.009>
35. Oparaji U, Sheu RJ, Bankhead M, Austin J, Patelli E. (2017). Robust artificial neural network for reliability and sensitivity analyses of complex non-linear systems. *Neural Networks* 96, 80–90. <https://doi.org/10.1016/j.neunet.2017.09.003>
36. Saenger E, Enzmann F, Keehm Y, Steeb H. (2011). Digital rock physics: Effects of fluid viscosity on effective elastic properties. *Journal of Applied Geophysics* 74, 4, 236–241. <https://doi.org/10.1016/j.jappgeo.2011.06.001>
37. Saenger E, Lebedev M, Uribe D, Osorno M, Vialle S, et al. (2016). Analysis of high-resolution X-ray computed tomography images of Bentheim sandstone under elevated confining pressures. *Geophysical Prospecting* 64, 4, 848–859. <https://doi.org/10.1111/1365-2478.12400>
38. Schepp L, Ahrens B, Balcewicz M, et al. (2020). Digital rock physics and laboratory considerations on a high-porosity volcanic rock. *Scientific Reports* 10, 5840. <https://doi.org/10.1038/s41598-020-62741-1>
39. Scherer C, Lavina E. (2006). Stratigraphic evolution of a fluvial–eolian succession: The example of the Upper Jurassic—Lower Cretaceous Guarú and Botucatu formations, Paraná basin, Southernmost Brazil. *Gondwana Research* 9, 4, 475–484. <https://doi.org/10.1016/j.gr.2005.12.002>

40. Schlüter S, Sheppard A, Brown K, Wildenschild D. (2014). Image processing of multiphase images obtained via X-ray microtomography: A review. *Water Resources Research*, 50, 4, 3615–3639. <https://doi.org/10.1002/2014WR015256>
41. Schön J. (2014). *Physical Properties of Rocks*. 2nd ed., Elsevier. Hardback ISBN: 9780081004043, eBook ISBN: 9780081004234. <https://shop.elsevier.com/books/physical-properties-of-rocks/schon/978-0-08-100404-3>
42. Seidl D, Valiveti D. (2022). Peridynamics and surrogate modeling of pressure-driven well stimulation. *International Journal of Rock Mechanics and Mining Sciences* 154, 105105. <https://doi.org/10.1016/j.ijrmms.2022.105105>
43. Shahin M. (2015). Use of evolutionary computing for modelling some complex problems in geotechnical engineering. *Geomechanics and Geoengineering* 10, 2, 109–125. <https://doi.org/10.1080/17486025.2014.921333>
44. Shang X, Liu Z, Zhang J, Lyu T, Zou Y. (2023). Tailoring the mechanical properties of 3D microstructures: A deep learning and genetic algorithm inverse optimization framework. *Materials Today*, 70, 71-81. <https://doi.org/10.1016/j.mattod.2023.09.007>
45. Singh A, Regenauer-Lieb K, Walsh S, Armstrong R, van Griethuysen J, et al. (2020). On Representative elementary volumes of grayscale micro-CT images of porous media. *Geophysical Research Letters* 47, 15. <https://doi.org/10.1029/2020GL088594>
46. Sun H, Belhaj H, Tao G, Vega S, Liu L. (2019). Rock properties evaluation for carbonate reservoir characterization with multi-scale digital rock images. *Journal of Petroleum Science and Engineering* 175, 654–664 <https://doi.org/10.1016/j.petrol.2018.12.075>
47. Synopsis, Inc. (2021). SimplewareTM ScanIP, version S-2021-06, Mountain View, USA. <https://www.synopsys.com/content/dam/synopsys/simpleware/pdfs/simpleware-s2021-06-lifesciences.pdf>
48. Vrugt J, Oliveira D, Schoups G, Diks C. (2022). On the use of distribution-adaptive likelihood functions: Generalized and universal likelihood functions, scoring rules and multi-criteria ranking. *Journal of Hydrology* 615, 128542. <https://doi.org/10.1016/j.jhydrol.2022.128542>
49. Vrugt J, Stauffer P, Wohling T, Robinson B, Vesselinov V. (2008). Inverse modeling of subsurface flow and transport properties: a review with new developments. *Vadose Zone Journal* 7, 2, 843–864. <https://doi.org/10.2136/vzj2007.0078>
50. Wang Y, Armstrong R, Mostaghimi P. (2019a). Enhancing resolution of digital rock images with super resolution convolutional neural networks. *Journal of Petroleum Science and Engineering* 182, 106261. <https://doi.org/10.1016/j.petrol.2019.106261>
51. Wang Y, Armstrong R, Mostaghimi P. (2019b). Boosting resolution and recovering texture of 2D and 3D micro-CT images with deep learning. *Water Resources Research* 56, 1. <https://doi.org/10.1029/2019WR026052>
52. Wetzell M, Kempka T, Kuhn M. (2020). Hydraulic and mechanical impacts of pore space alterations within a sandstone quantified by a flow velocity-dependent precipitation approach. *Materials* 13 (14), 3100. <https://doi.org/10.3390/ma13143100>
53. Yang J, Liu Y, Yagiz S, Laouafa F. (2021). An intelligent procedure for updating deformation prediction of braced excavation in clay using gated recurrent unit neural networks. *Journal of Rock Mechanics and Geotechnical Engineering* 13, 6, 1485–1499. <https://doi.org/10.1016/j.jrmge.2021.07.011>